ASTROSAT/LAXPC REVEALS THE HIGH-ENERGY VARIABILITY OF GRS 1915+105 IN THE χ CLASS

J S Yadav[1], Ranjeev Misra[2], Jai Verdhan Chauhan[1], P C Agrawal[3], H M Antia[1], Mayukh Pahari[2], Dhiraj Dedhia[1],
Tilak Katoch[1], P. Madhwani[1], R K Manchanda[4], B Paul[5], Parag Shah[1], and C H Ishwara-Chandra[6]

[1] Tata Institute of Fundamental Research, Homi Bhabha Road, Mumbai, India; jsyadav@tifr.res.in
[2] Inter-University Centre for Astronomy and Astrophysics, Pune 411007, India
[3] UM-DAE Center of Excellence for Basic Sciences, University of Mumbai, Kalina, Mumbai-400098, India
[4] University of Mumbai, Kalina, Mumbai-400098, India
[5] Department of Astronomy and Astrophysics, Raman Research Institute, Bengaluru-560080 India
[6] National Center for Radio Astrophysics, Pune 411007, India
Received 2016 June 23; revised 2016 August 22; accepted 2016 August 23; published 2016 December 5

ABSTRACT

We present the first quick look analysis of data from nine *AstroSat*'s Large Area X-ray Proportional Counter (LAXPC) observations of GRS 1915+105 during 2016 March when the source had the characteristics of being in the Radio-quiet χ class. We find that a simple empirical model of a disk blackbody emission, with Comptonization and a broad Gaussian Iron line can fit the time-averaged 3–80 keV spectrum with a systematic uncertainty of 1.5% and a background flux uncertainty of 4%. A simple dead time corrected Poisson noise level spectrum matches well with the observed high-frequency power spectra till 50 kHz and as expected the data show no significant high-frequency (>20 Hz) features. Energy dependent power spectra reveal a strong low-frequency (2–8 Hz) quasi-periodic oscillation and its harmonic along with broadband noise. The QPO frequency changes rapidly with flux (nearly 4 Hz in $\sim$5 hr). With increasing QPO frequency, an excess noise component appears significantly in the high-energy regime (>8 keV). At the QPO frequencies, the time-lag as a function of energy has a non-monotonic behavior such that the lags decrease with energy till about 15–20 keV and then increase for higher energies. These first-look results benchmark the performance of LAXPC at high energies and confirms that its data can be used for more sophisticated analysis such as flux or frequency-resolved spectro-timing studies.

Key words: accretion, accretion disks – black hole physics – X-rays: binaries

1. INTRODUCTION

The extraordinary micro-quasar black hole system, GRS 1915+105 was the primary subject of a large number of *Rossi X-ray Timing Explorer* (*RXTE*) observations that has revealed its complex spectral and timing behavior, which needs to be classified into more than 12 distinct variability classes (Belloni et al. 2000). It is the first Galactic black hole X-ray binary where superluminal jet have been discovered (Fender et al. 1999). Extensive study revealed variations in its radio flux (at 15.2 GHz) from few to few hundreds of milliJy in different variability classes (Muno et al. 2001) as well as in the same variability class (Pahari et al. 2013b). This source has been extensively studied to understand the disk-jet connection in X-ray binaries (Mirabel et al. 1998; Yadav 2001; Fender & Belloni 2004; Yadav 2006).

During some of these classes, the source shows large amplitude variability in flux and spectral shape on timescales of minutes to hours (Taam et al. 1997; Paul et al. 1998; Yadav et al. 1999; Pahari et al. 2013a, 2013c), while in others the source is relatively steady. Even when the source is relatively quiet on minute timescales, detailed analysis often shows strong coherent quasi-periodic oscillations (QPOs) with frequencies of the order of a few Hz (Morgan et al. 1997; Paul et al. 1997; Muno et al. 1999; Pahari et al. 2013b). Interestingly, one of the promising models for these oscillations is that the variation is produced by the inner disk globally precessing due to the Lens–Thirring effect around a spinning black hole (Stella & Vietri 1998; Ingram et al. 2009). Evidence for such a behavior is inferred from the time-averaged spectrum and the variation of the QPO properties with intensity and corresponding spectral parameters (Ingram & van der Klis

2015). Perhaps more importantly, energy dependent QPO properties such as fractional rms and time-lag between different energy bins provide crucial information regarding such phenomena (Reig et al. 2000; Muno et al. 2001; Qu et al. 2010; Pahari et al. 2013b).

Most of the combined spectral and timing analysis of such sources, like GRS 1915+105, has been done using the *RXTE* Proportional Counter Array (PCA) data, which despite the wealth of information they provided, were limited due to several reasons. Due to telemetry constraints, the *RXTE* data of bright sources on many occasions were binned in channels on board, leaving only a few broad energy bands for which analysis could be undertaken. The effective area of the proportional counter units (PCUs) decreased rapidly beyond 30 keV (Jahoda et al. 2006) and hence the statistics for high-energy photons were usually not sufficient to do any detailed timing analysis. Despite efforts to improve the calibration (Shaposhnikov et al. 2012), the spectral analysis was typically limited to the 3–30 keV band and hence one had to rely on rare simultaneous observations of the source from other satellites to obtain broadband spectral data.

AstroSat, the first Indian astronomical satellite, which was successfully launched on 2015 September 28, has five scientific instruments on board (Agrawal 2006; Singh et al. 2014). One of the primary instruments is the Large Area X-ray Proportional counters (LAXPC) which consists of three identical PCUs adding up to an effective area of $\sim$6000 cm^2 at 15 keV (Yadav et al. 2016; P. C. Agrawal 2016, in preparation). After launch, LAXPC went through a series of performance verification tests, where it observed different blank sky coordinates, standard sources, and sources of scientific interest. These tests have allowed for the calibration and estimation of

Table 1
Comparison of Approximate LAXPC Characteristics with Those of *RXTE/*PCA and *NuSTAR*

Instrument	*AstroSat/* LAXPC (i)	*RXTE/*PCA (ii) & (iii)	*NuSTAR* (iv) & (v)
Detector type	Non–imaging	Non–imaging	Imaging
Energy range (keV)	3–80	2–60	3–78
Dead time	$\sim$42 μs	$\sim$10 μs	1–2 ms
Energy Resolution			
At 6 keV	$\sim$20%	$\sim$18%	$\sim$6.67%
At 60 keV	$\sim$10%	...	$\sim$1.5%
Effective area (cm^2)[a]			
At 10 keV	$\sim$6100	$\sim$7000	$\sim$800
At 30 keV	$\sim$4500	$\sim$1000	$\sim$300
At 50 keV	$\sim$5100	$\sim$750	$<$200

Note.
[a] The LAXPC effective area quoted here is based on the simultaneous fit to LAXPC and *NuSTAR* data. A more reliable estimate will be available after simultaneous observations with several observatories are performed. References: (i) Yadav et al. (2016), (ii) Zhang et al. (1993), (iii) Jahoda et al. (2006), (iv) Harrison et al. (2013), (v) Bachetti et al. (2015).

the instrument spectral response, background characteristic, and timing capabilities, which will be presented in detail elsewhere. Here we provide a first estimate of the characteristics of the instrument and compare them with those of *RXTE/*PCA and *NuSTAR* in Table 1. While *NuSTAR* is an imaging instrument, the LAXPC provides several advantages as compared to the *RXTE/*PCA. The effective area of the LAXPC at energies greater than 30 keV is significantly larger than the PCA (Table 1). The complete event data obtained allows for an energy dependent analysis of any choice of energy bins. The other co-pointing instruments on board *AstroSat*, especially the Soft X-ray telescope (SXT), can provide critical spectral coverage below 3 keV.

As a part of the performance verification, during 2016 March 5–7, *AstroSat* observed the black hole system GRS 1915+105 for many orbits and for nine of them the flux was relatively steady on timescales of minutes suggestive that they belong to the Radio-quiet χ class. GRS 1915+105 moves to this class from the θ class and at the end of the χ class, the source again returned to the θ class. Therefore, GRS 1915+105 remains for $\sim$14 hr in the Steep Power Law (SPL) state, which is a subclass of the χ class. X-ray activity in GRS 1915+105 has been classified into 12 different classes. χ class is characterized by hard spectrum with low-frequency QPO, while θ class is a flaring X-ray class associated with transient radio jets every 20–30 minutes (Belloni et al. 2000).

In this work, we present the first-look spectral and timing analysis of these observations, with particular emphasis on the high-energy behavior.

2. SPECTRAL ANALYSIS

In this work, we present an analysis of nine LAXPC observations of GRS 1915+105 as listed in Table 2. Each of them were obtained from a single orbit with effective exposure of $\sim$1–3 ksec each. A typical 1 ksec light curve observed during orbit no. 2363 is shown in Figure 1, where the count rate from all three LAXPC units are combined. We begin with

the time-averaged spectral analysis of these observations. While the complete detailed description of LAXPC performance and calibration will be presented elsewhere (Yadav et al. 2016), here we highlight some of the basic points. The response function for each of the LAXPC units was computed using GEANT4 simulations.

Most of the background is coming from the cosmic diffused X-ray background. The background for each of the units was modeled as a function of the latitude and longitude of the satellite (H. M. Antia 2016, in preparation). There are differences between the observed background and the model at a level of about 4%, which is not understood so far. In this work, the timing analysis is for frequencies much larger than 0.01 Hz and the background is stable on these timescales. We have checked that the power spectra for Crab and the background show no spurious signals at these frequencies. The source spectra, light curves and background spectra were extracted using software that will become part of the standard pipeline for the LAXPC. The spectral fitting was done using the XSPEC v 12.8.1g spectral fitting package.

The LAXPC consists of three identical proportional counter detector units, which are named LAXPC10, LAXPC20, and LAXPC30. We checked that joint spectral fitting of LAXPC10 and simultaneous *NuSTAR* observations of Crab produced the expected best-fit power-law index of 2.08 ± 0.01 with the normalization constant of LAXPC relative to *NuSTAR* giving the effective area quoted earlier. For the fitting, a 4% uncertainty was added to the background (which needs to be dead time corrected for bright sources) and a 1.5% overall systematic is added to the spectrum to account for the uncertainty in the response. We use these values throughout this work. The complete energy spectrum of the LAXPC 10 was represented by 512 pha bins of which 292 of them lie within the energy range of 3–80 keV. This gives an average energy bin size of $\sim$0.3 keV, which is approximately a fourth of the approximate energy resolution of LAXPC at 6 keV i.e., $\sim$1.2 keV. However, at higher energies the spectra would be oversampled and more detailed later work should rebin the spectra based on the energy resolution, once the response of the detector is better understood and modeled.
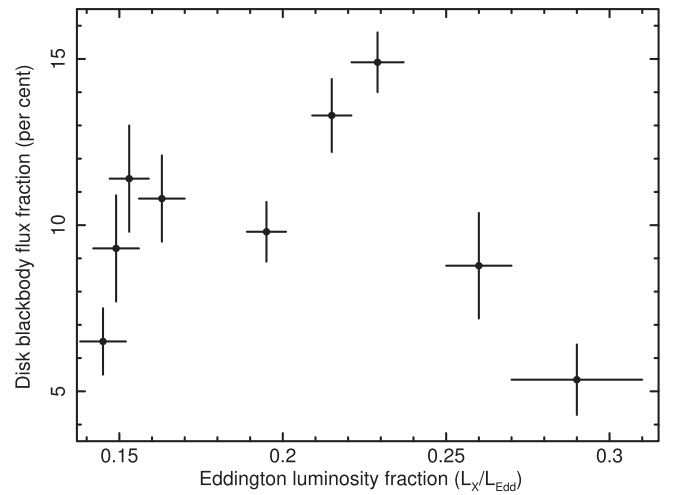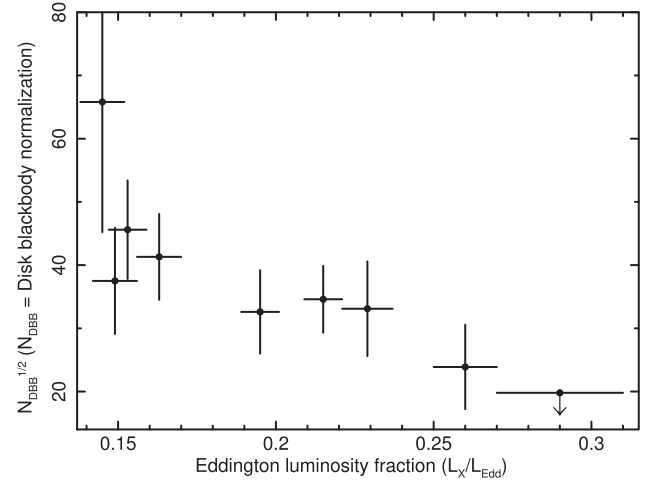
Figure 2 shows the counts spectrum of LAXPC10 for the observation of orbit no. 2363, which was fitted by a model consisting of a disk blackbody Component (XSPEC model DISKBB), a thermal Comptonized component (XSPEC model NTHCOMP), and a broad Gaussian feature (XSPEC model GAUSSIAN) to represent the Iron line. The disk blackbody component was taken to be the seed photon source for the Comptonization. All spectra are modified by the presence of neutral hydrogen absorption, which has been taken care of by using the TBabs model (Wilms et al. 2000). GRS 1915+105 has high intrinsic absorption with an equivalent neutral column density of the order of few times 10^{22} cm^{-2} (e.g., McClintock et al. 2006). The LAXPC data is sensitive only beyond 3 keV, making it difficult to constrain the column density and hence it was fixed to a value of 6×10^{22} cm^{-1}. The thick blue line represents the expected background count rate for the observation. The bottom panel shows strong residuals, which may be due to uncertainties in the response function. Indeed, if an overall systematic of 1.5% is added (with 4% uncertainty in the background), the fitting gives an acceptable $\chi^2/\mathrm{dof} = 278/284$ in place of $\chi^2/\mathrm{dof} = 1048/284$ (without the systematic). Some of the parameters obtained were the disk

Table 2
LAXPC Observation Details of GRS 1915+105

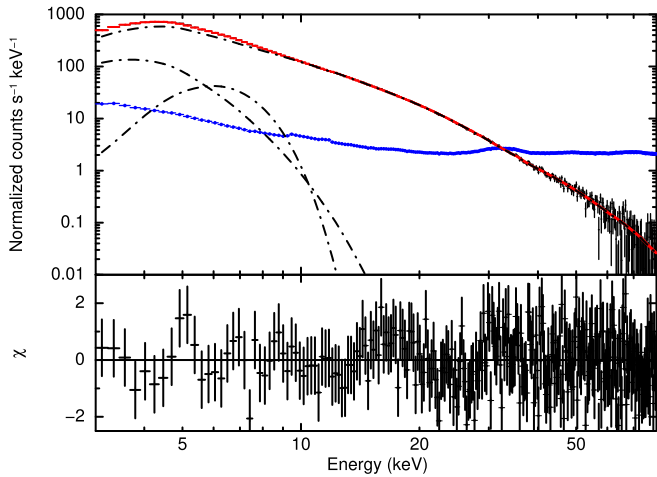| Orbit number	Date	Start time (hh:mm:ss)	Effective on-source exposure (s)	Average source count rate of LAXPC10	QPO frequency (Hz)
2359	05 Mar 2016	09:54:19.24	1728.0	3697 ± 30	5.72 ± 0.04
2360	05 Mar 2016	11:33:47.19	721.0	3637 ± 30	6.55 ± 0.05
2361	05 Mar 2016	13:12:31.66	1439.0	2855 ± 30	4.53 ± 0.03
2362	05 Mar 2016	14:54:35.59	2165.0	2400 ± 26	3.49 ± 0.03
2363	05 Mar 2016	16:23:03.34	2292.0	2209 ± 11	2.53 ± 0.02
2364	05 Mar 2016	18:08:11.91	2716.0	2219 ± 12	2.79 ± 0.03
2365	05 Mar 2016	19:48:03.92	3148.0	2313 ± 19	3.18 ± 0.03
2367	05 Mar 2016	23:35:54.71	1913.0	3022 ± 24	4.61 ± 0.03
2368	06 Mar 2016	01:34:36.34	2873.0	3334 ± 27	4.94 ± 0.04
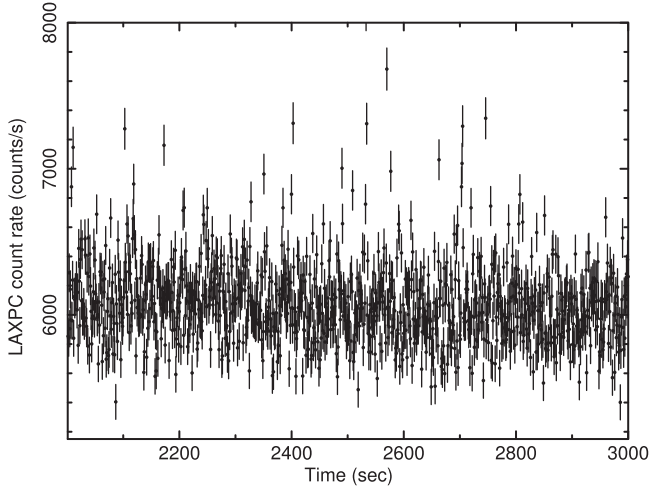
Figure 1. Typical 1 ksec light curve of the χ class in the energy range of 3.0–80.0 keV is shown where count rate from all three LAXPC detectors— LAXPC10, LAXPC20, and LAXPC30 are combined.

Figure 2. Top panel shows counts spectrum as observed from LAXPC10 for the orbit number 2363, fitted with a model consisting of a disk blackbody, thermal Comptonization and a broad iron line. Resultant model spectra is shown by the red line, while the thick blue line represents the expected background level. The bottom panel shows the residuals, which may be due to systematic errors in the response function. The spectrum provides a good fit of $\chi^2/\mathrm{dof} = 278/284$ when a 1.5% systematics are added and the background uncertainty is taken to be 4%.

temperature $kT = 0.88^{+0.05}_{-0.08}$ keV, the Comptonization photon index $\Gamma = 2.57^{+0.03}_{-0.02}$, and electron temperature $kT_e = 16.8^{+1.05}_{-1.28}$ keV. Similar fits were obtained for all nine


Figure 3. Square root of disk blackbody normalization (top panel) and the percentage fraction of the disk to the total flux as a function of the Eddington ratio (bottom panel) are shown for different observations. For computing the Eddington ratio, we used a black hole mass of $12.5 M_\odot$ and a distance to the source $D = 9$ kpc (Reid et al. 2014).

observations. While detailed tabulation of the best-fit spectral parameters using different spectral models will be shown elsewhere, here we highlight some of the generic results. The normalization of the disk blackbody emission seems to decrease slightly with luminosity (top panel of Figure 3), but the large errorbars do not allow for concrete statements to be made. For the mass and distance assumed for this source, the typical value of the normalization would imply an inner radius
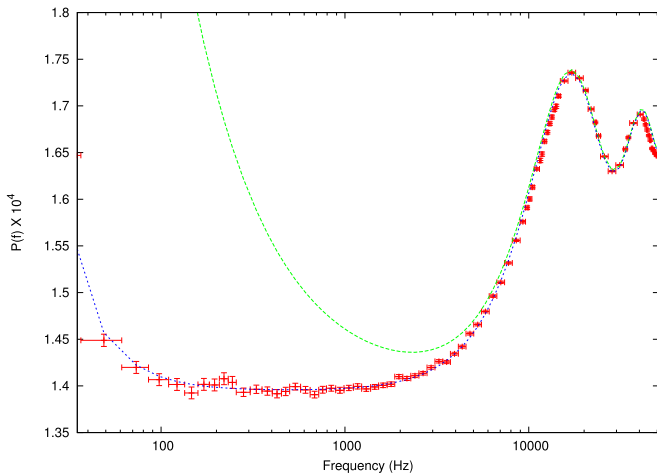
Figure 4. High-frequency rebinned power spectra for a 2.3 ksec observation of GRS 1915+105 in the χ class. The power spectra matches well with the predicted Poisson noise level with a dead time of $\tau = 42.3$ microseconds and a low-frequency power-law component. The green line shows the expected peak power of a QPO with quality factor $Q = 4$ and rms of 5%. LAXPC would have detected a QPO of such a strength easily till 3000 Hz.

of $\sim 6(f/1.7)^2 GM/c^2$ for a color factor $f \sim 1.7$ (Shimura & Takahara 1995), suggesting that disk extends to be truncated for a fast spinning black hole (McClintock et al. 2006). Moreover, for the nine observations, the temperature of the Comptonizing medium was found to be around ~ 15 keV. The fraction of the disk component flux to the total does not seem to show any correlation as shown in the bottom panel of Figure 3. However, more detailed investigations taking into account more physical models like gravitationally smeared disk and Iron line emission (instead of the simple DISKBB model and broad Gaussian used here) need to be undertaken before any inferences can be made. We defer such analysis to future when we expect to have significantly better instrument response and background modeling than the currently available version.

3. VARIABILITY ANALYSIS

3.1. High-frequency Variability

The high telemetry of *AstroSat* allows for LAXPC data to be obtained in event mode for high count rate sources at the instrument time resolution. This provides an unprecedented opportunity to study the rapid variability of bright sources.

As an example to demonstrate the capability of LAXPC to detect high-frequency variability, we consider just one observation of effective exposure ~ 2.3 ksec, i.e., orbit no. 2363. Using the event mode data at the time resolution of 10 microseconds, the power spectrum up to a Nyquist frequency of 50 kHz was computed for counts in the energy range of 3.0–80.0 keV. Data from all three units were combined. The light curve was divided into segments of 2048 bins corresponding to 0.02048 s. The total exposure consists of 97655 segments. The power spectrum generated at 1024 frequency points was rebinned and shown in Figure 4. The rise in the power spectrum at low frequencies (<60 Hz) is due to low-frequency variability of the source, while the structure at high frequencies is due to the characteristic effect of dead time. The expected dead time corrected Poisson level power for a system, which is non-paralyzable is given by

Zhang et al. (1995)

$$P_N(f) = \frac{1}{R_{BO}^2}\left[2 + 4\frac{\langle R_B \rangle}{R_T}\right.$$

$$\left. \times \frac{-1 + \cos(2\pi f\tau_d) - (2\pi f\tau)\sin(2\pi f\tau_d)}{2 + (2\pi f\tau)^2 - 2\cos(2\pi f\tau_d) + 2\pi f\tau\sin(2\pi f\tau_d)}\right]. \quad (1)$$

Here, τ_d is the dead time and R_{BO} is the observed rate in the energy band being considered. R_T is the dead time corrected observed count rate for the detector, i.e., $R_T = R_{TO}/(1 - R_{TO}\tau_d)$, where R_{TO} is the observed total count rate and $\tau = 1/R_T$. $\langle R_B \rangle$ is the average dead time corrected count rate per detector, i.e., $\langle R_B \rangle = R_{BO}(1 + R_T\tau_d)/N_{pcu}$ with N_{pcu} being the number of LAXPC units being considered.

For the low-frequency variability, we consider a power law of $\propto f^{-2}$ and hence the total function is taken to be $P(f) = A(f/10\ \text{Hz})^{-2} + P_N(f)$ and we fit the unbinned observed power spectrum consisting of 1024 frequency bins. The mean effective dead time as measured on the ground was around 50 microseconds, but it has variations depending on the kind of event detected and hence is not a constant as assumed in the above equation. Hence, we attempt to obtain an average value of dead time by fitting the parameters, A and τ_d and keeping the rest of the parameters fixed at their observed values, i.e., $R_{BO} = 5999.7$ and $R_{TO} = 6236.4$ counts s^{-1}. The fit gave a χ^2/dof $= 2349.8/1022$ or a reduced $\chi^2_{red} = 2.3$. The best-fit average dead time was found to be $\tau_d = 42.3$ microseconds. The best-fit curve is shown as a dotted blue line in Figure 4. Thus, considering all the uncertainties, the expected dead time corrected power spectrum is remarkably close to the observed one. In fact, a 0.5% systematic uncertainty added in quadrature to the power spectrum yields a reduced $\chi^2_{red} = 0.7$, showing the level at which the power spectrum can be trusted in these high frequencies. The sensitivity of the instrument can be further seen by the dotted line in Figure 4, which represents the expected peak of the power spectrum for a Lorentzian shaped QPO, with a quality factor $Q = 4$ and rms of 5%, i.e., $P_{QPO} = \frac{2Q}{\pi f}(\text{rms})^2$. Thus, a QPO of this strength and quality factor would have easily been detected by LAXPC for a source like GRS 1915+105 in a 3 ksec observation if its frequency was less than 3000 Hz.

Since high-frequency features when seen in black hole systems are stronger at higher energies and sometimes can only be detected at high energies (Cui et al. 2000; Homan et al. 2003), we verify LAXPC capability to detect such QPOs in the 20–80 keV band. In this band for the observation under consideration the count rate observed was 396 counts s^{-1}. Figure 5 shows the rebinned power spectrum and the expected Poisson noise level at this energy band. While some features can be seen, they are not significant in the sense that a fit to the power spectrum using just the noise level and low-frequency component, gives a reduced $\chi^2_{red} = 1.05$. The expected peak power for a QPO with the quality factor $Q = 4$ and rms 5% (green line in Figure 5) shows that such a QPO would have been only marginally detected by LAXPC for this observation.

3.2. Hardness intensity and Color–Color Variations

Having established the expected result that the source does not show any strong high-frequency phenomena, we turn our attention to the behavior of the source in low frequencies i.e., <10 Hz. To begin, we compute hardness intensity and color–color plots to understand the overall spectral variability of the
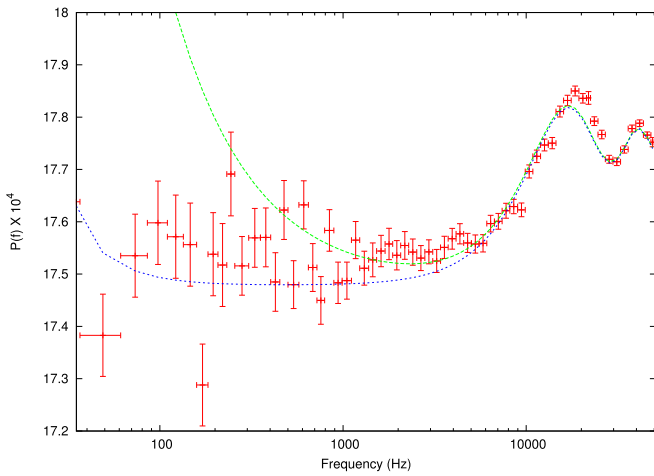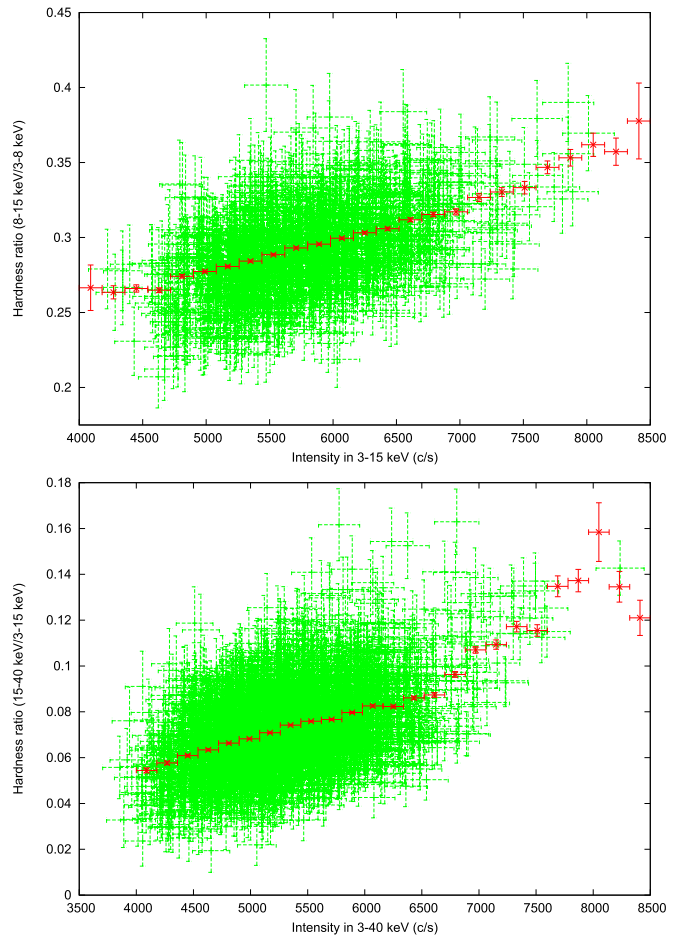
Figure 5. Same as Figure 4, except that the power spectrum and the expected dead time corrected Poisson level is computed for counts in the high-energy 20–80 keV band. While there are hints of possible features they are not significant.


Figure 6. Hardness intensity plot for 2.3 ksec observation of GRS 1915+105 in 0.25 s time bin. About 20% of the total points are shown for clarity. In the top panel, the hardness is defined as the count rate ratio between 8–15 and 3–8 keV bands, while the intensity is the total count rate in the 3–15 keV band. In the bottom panel, the ratio is similarly defined for 3–15 and 15–40 keV and the total intensity in the 3–40 keV band. The red points are the average values at a given intensity. The source clearly shows increasing hardness with intensity in both soft and hard bands.

source. Light curves were extracted from all three units in different energy bands and the dead time corrected background in that band (i.e., $R_{BC} = R_B/(1 + R_T \tau_d)$) was subtracted.

The top panel of Figure 6 shows the hardness ratio between the 8–15 and 3–8 keV band versus the intensity in the 3–15 keV with a time bin of 0.25 s. The source clearly hardens as it gets brighter, which is better illustrated when the points corresponding to an intensity bin are averaged (solid line in the figure). More remarkable is that LAXPC allows a hardness intensity plot to be made in a broader energy ranges of 3–15 and 15–40 keV bands as shown in the bottom panel of Figure 6. The behavior of the source is found to be similar to the softer bands. That such an analysis can be undertaken shows that LAXPC data is well suited for more sophisticated analysis such as flux or even frequency-resolved spectroscopy, which will be undertaken in a future work.

3.3. Energy Dependent Power Spectra

The LAXPC observations allow for the computation of power spectra in different energy bands. As an illustration, in Figure 7, the power spectra in three energy bands—3.0–8.0 (left column), 8.0–20.0 (middle column), and 20.0–80.0 keV (right column) are shown for three representative observations. The dead time ($\sim$42 μsec) corrected Poisson noise level has been subtracted from each power spectrum. The low-energy power spectra clearly shows a QPO at 2–7 Hz along with a harmonic for some of the observations, which are fitted using Lorentzians. Complex broadband continuum noise is seen for all the spectra, which has been empirically fitted using a broken power law and a few broadband Lorentzians depending on the energy. The bottom panels show residuals in terms of χ and it is clear that the high-quality data require more sophisticated analysis rather than the empirical one adopted here. In particular, the power spectra, as well as the QPO frequencies, would not be stationary even during a single observation and dynamical or flux resolved power spectra are needed to quantify the changes. While deferring such a detailed analysis for later, here we bring out the broad results that the QPO is detected at high energies and that the shape of the power spectrum significantly evolves with energy. The shape changes with frequency of the QPO and there is an additional broad

noise component particularly at 8–20 keV for high QPO frequencies. Such detailed energy dependent power spectra is a significant improvement over the earlier *RXTE* results. As expected the QPO frequency varies with flux as shown in Figure 8, which shows the QPO frequency as a function of the Eddington fraction. It is quite remarkable that the frequency changed by about 4 Hz with near doubling of the luminosity in a relatively short time of $\sim$5 hr (as shown in Table 2).

3.4. Energy Dependent Time Lag

The complete event mode data obtained from LAXPCs allows time-lags to be computed between different user chosen energy bands. This is demonstrated in Figure 9, where the middle column shows the measured time-lag at the QPO frequency for the three representative observations. The complete power spectra for 3–80 keV is shown in the left column. The time-lag is with reference to the 3–4 keV band and choice of energy bins is arbitrary. The time lags have a non-monotonic nature in the sense that typically the photons of $\sim$15 keV arise before the low-energy ones (i.e., a soft lag) but for higher energies the time lag decreases, i.e., typically the 50 keV photons have significantly less lag. The background
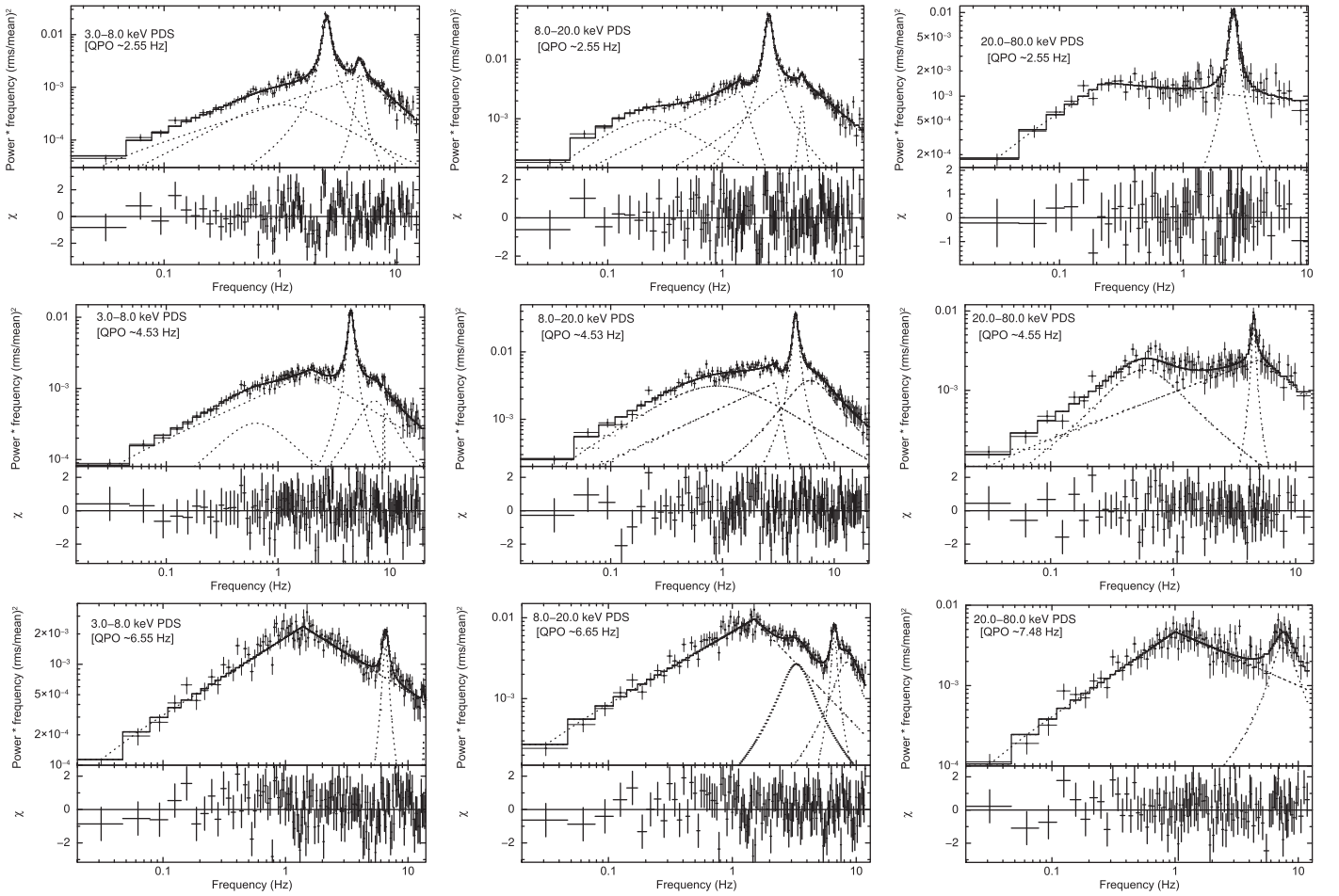
Figure 7. Power density spectra at three different energy bands 3.0–8.0 keV (first column), 8.0–20.0 keV (second column), and 20.0–80.0 keV (third column) are shown for three observations when strong QPOs are detected at ∼2.55 Hz (top row), ∼4.53 Hz (middle row), and ∼6.55 Hz (bottom row) respectively. Due to observed break in noise continuum, the broken power-law model is used to fit the noise component, while Lorentzians are used to fit QPO and harmonic features. It may be noted that a significant, excess noise component (modeled with broad Lorentzian) appears in the PDS with higher QPO frequencies at the energy >8.0 keV. Such features were not detected by *RXTE* due to its highly reduced efficiency in 8.0–20.0 keV energy band.
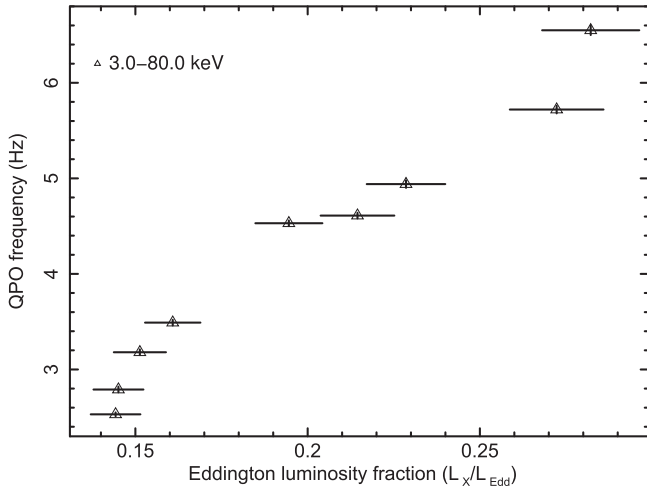

Figure 8. Primary QPO frequency is shown as a function of the ratio of source luminosity to Eddington luminosity. QPO frequency is observed to be monotonically increasing with the source luminosity.

corrected rms variability of the QPO increases till about ∼15 keV and then seems to saturate as shown in the right column of Figure 9. However, while the QPO is detected at high energies and hence the time-lag measurements, the 4%

uncertainty in the background rate does not allow for accurate measurement of the normalized rms above ∼30 keV. This may improve once more accurate background models are available. While the energy dependent time-lag for energies <20 keV is qualitatively similar to that observed by *RXTE* (Qu et al. 2010; Pahari et al. 2013b), LAXPC reveals that their behavior changes dramatically for high energies. Time-lag measurements may suffer from instrumental behavior such as dead time or other such effects, which may produce fake correlations between count variation in different energy bands. The completely independent electronics of the different detectors in the LAXPC instrument allows one to check if such effects are affecting the results. In Figure 10, the time-lags for the ∼2.55 Hz are again measured as a function of energy but here the reference band (3–4 keV) is taken from LAXPC10 and the others from LAXPC20 (black points) and vice versa (red points). The behavior of the energy dependent time lag is reproduced in the cross PCU analysis giving confidence that the overall results obtained from the combined analysis is correct.

For the QPO observed at ∼2.55 Hz, the next harmonic is detected clearly in high-energy bins and thus one can measure as shown in the left panel of Figure 11, the time-lag as function of energy for both the QPO and its harmonic. As was known
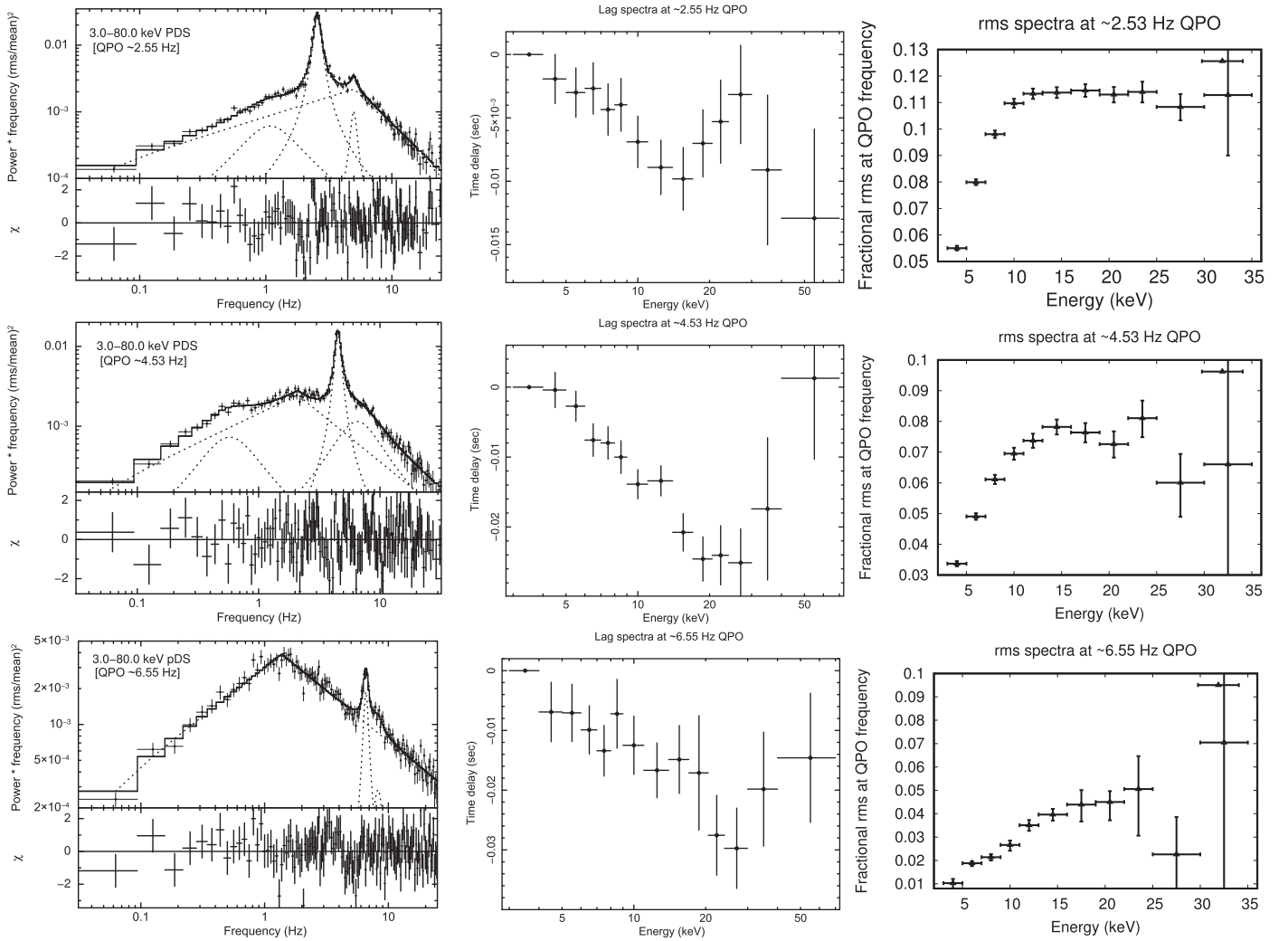
Figure 9. In each row, 3.0–80.0 keV fitted power density spectrum in the frequency range of 0.1–10.0 Hz along with its residual (first column), time-lag spectra at the corresponding fundamental QPO frequencies (second column) and fractional rms spectra at the same QPO frequencies (third column) are shown. PDS, time-lag, and rms spectra are calculated at ~2.55 Hz (top rows), ~4.53 Hz (middle rows), and ~6.55 Hz (bottom rows) respectively. In all lag spectra, the 3.0–4.0 keV band is considered to be the reference band.
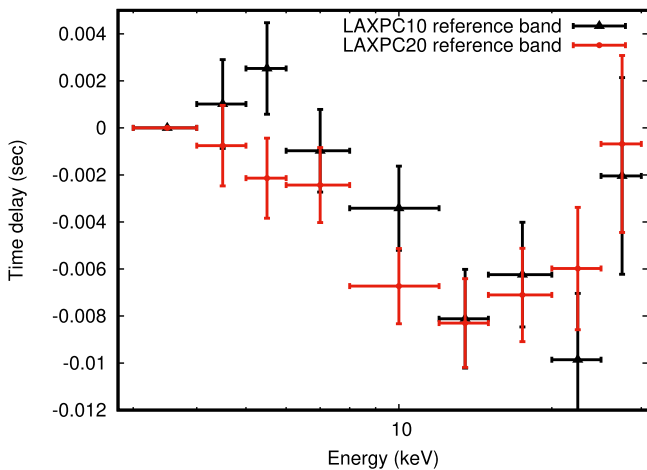
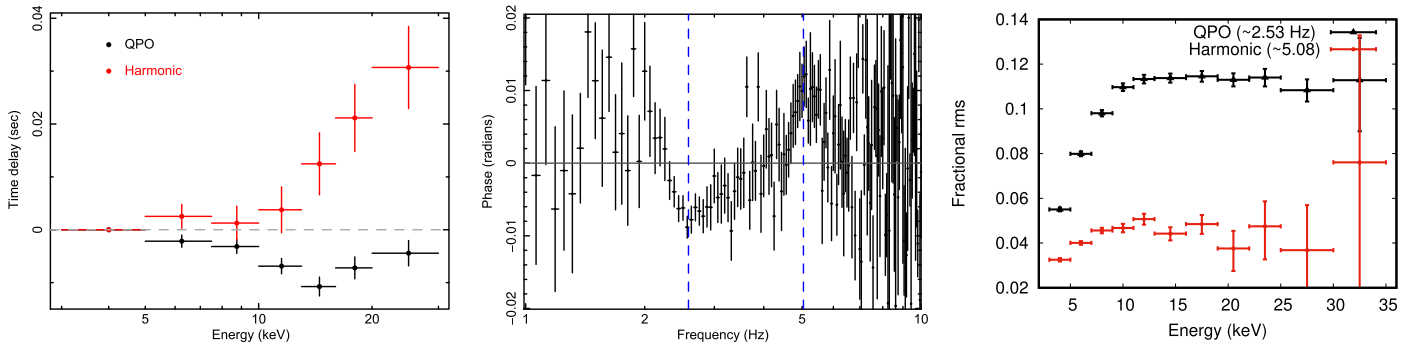**Figure 10.** Time-lag spectra at ~2.55 Hz QPO frequencies from two LAXPC units, where lag-spectra of second LAXPC unit (LAXPC20; black points) is computed by choosing the reference band from the first LAXPC unit (LAXPC10) and vice versa (red points). The similarity between these curves and for the combined data (top middle panel of Figure 9) shows that instrumental effects such as dead time are not affecting the results.

before for low energies using *RXTE* data (Pahari et al. 2013b), the time lag for the harmonic is of the opposite sign (i.e., the time lag is hard) as compared to the fundamental where the time-lag is soft. The time lags, $\Delta\tau$, or more conveniently the phase lags $\Delta\phi = 2\pi f \Delta\tau$ can also be measured as a function of frequency f, which is shown in the middle panel of Figure 11. Here the lag is measured between 10–20 keV band and the 3–5 keV band, where the choice of energy bands is motivated by the shape of the energy dependent time lag of the QPO. The soft phase lag at the QPO frequency of 2.55 Hz is clearly seen in Figure 11 while the phase lag is positive at its harmonic of 5.03 Hz. The right panel of Figure 11 shows the variation of the fractional rms of the QPO and the next harmonic.

4. SUMMARY AND DISCUSSION

In this work, we have presented the first-look analysis of nine orbits of *AstroSat*/LAXPC data of GRS 1915+105, which resulted in nine observations with exposures varying between 700 and 3200 s. The primary results are as follows.

(1) The energy spectra for each observation can be well fitted by an empirical model consisting of a disk blackbody,

Figure 11. Left panel shows energy dependent time-lag spectra at ~2.55 Hz fundamental QPO frequency (black circles) and 5.08 Hz harmonic frequency (red circles) respectively. While soft lag is observed at QPO frequency, the lag spectra clearly show hard lag at harmonic frequency. The middle panel shows phase-lag spectra as a function of Fourier frequency, where the phase lag is computed between 3.0–5.0 keV and 10.0–20.0 keV energy bands. The position of ~2.55 Hz QPO and its harmonic at ~5.03 Hz are shown by vertical dotted lines. Clearly, a phase rotation from negative at QPO frequency to positive at harmonic frequency is visible. The right panel shows fractional rms spectra at the fundamental QPO frequency (black) and its harmonic (red).

thermal Comptonization, and an iron line represented by a broad Gaussian. The systematic uncertainty of 4% for the background and 1.5% for the response provided acceptable fits to all spectra, which benchmarks LAXPC spectral capabilities.

(2) For a single ~3 ksec observation, the high-frequency power spectrum from 100–50,000 Hz, can be described by a simple dead time model with an effective dead time of 42.3 microseconds. Moreover, it is shown that a QPO with quality factor ~4 and fractional rms of 5% would have been detectable easily till 3000 Hz.

(3) Using 0.25 s time bins, hardness intensity and color–color diagrams for a ~3 ksec observations can be generated using not only soft but also hard (e.g., 15–40 keV) bands. The source shows increasing hardness with intensity in both soft and hard bands.

(4) Power spectra for three energy bins 3–8, 8–20, and 20–80 keV for each observation shows a prominent QPO, whose frequency varies from 2.55 to 6.55 Hz as the flux increases by a factor of 2 on a 6 hr timescale. The broadband continuum noise is complex and shows variation with flux as well as with energy. For example, a significant excess noise component appears for higher QPO frequencies in the 8–20 keV band.

(5) At the QPO frequency, the time-lag with respect to the 3–4 keV band decreases with energy till ~20 keV as expected from earlier *RXTE* results for the radio-quiet χ class of GRS 1915+105. LAXPC larger effective area at higher energies reveals that the lags are non-monotonic and beyond ~20 keV the time lag increases with energy. The time-lag for the next harmonic has the opposite sign as the fundamental and does not seem to roll over at high energies. Since the electronics of the PCUs are independent, we have confirmed the time-lag behavior using one PCU for the reference band and the another for the different bands.

During the nine observations with LAXPC, we infer that GRS 1915+105 was in the Radio-quiet χ class (SPL subclass). There are three characteristics of these observations that are consistent with earlier detection of this class with *RXTE*. Namely, (1) the Radio-quiet χ class shows a QPO with frequencies always higher than ~2.1 Hz and the time lag spectra at QPO frequencies always show a soft lag (Pahari et al. 2013b), (2) near-simultaneous measurement of Radio flux density using the Giant Meterwave Radio Telescope (GMRT)

at 610 MHz yielded a value of ~6.3 mJy, which is similar to that observed during Radio-quiet χ class (see the right panel of Figure 1 in Pahari et al. 2013b), and (3) the phase lag between two energy bands as a function of Fourier frequency is similar to that observed from Radio-quiet χ class.

These results benchmark the performance of LAXPC as well as bring out interesting first results which highlight the utility of LAXPC's larger effective area at high energies and event mode data. For example, the extension of the variation of the time lag to high energies brings out the potential to uncover the actual mechanism of the QPO. The QPO could be due to the precession of the inner disk due to the Lense–Thirring effect and in that case the time-lag may be due to light travel time effects of the irradiation by the inner disk on the non-precessing outer one (Stella & Vietri 1998; Ingram et al. 2009). The turn over of the time-lag at high energies would then suggest that perhaps it is due to the reflection bump being prominent at those energies and hence the delay with respect to the continuum at ~20 keV. Detailed spectroscopic information regarding the contribution of the reflection component in high energies and the expected light travel time-delays can reveal whether such a picture is correct or not. Alternatively, in an entirely different scenario, the QPO could be due to accretion rate variations, which induces a delayed response of the inner disk radius. Such a model successfully predicts similar non-monotonic behavior of the time-lag and rms for the fundamental and next harmonic for mHz QPO of the same source (Mir et al. 2016). Again detailed analysis taking into account the time-averaged spectrum needed to be undertaken to find whether such a model is also valid for QPOs with frequencies of few Hz.

A reanalysis of the data presented with more sophisticated spectral fitting along with data from the SXT on board *AstroSat*, as well as more detailed timing analysis such as dynamic power spectra, flux, and frequency-resolved spectroscopy, will provide unprecedented insight into the temporal behavior of GRS 1915+105 and other black hole systems.

observations possible. GMRT is run by the National Centre for Radio Astrophysics of the Tata Institute of Fundamental Research.

REFERENCES

Agrawal, P. C. 2006, AdSpR, 38, 2989
Bachetti, M., Harrison, F. A., Cook, R., et al. 2015, ApJ, 800, 109
Belloni, T., Klein-Wolt, M., Meńdez, M., van der Klis, M., & van Paradijs, J. 2000, A&A, 355, 271
Cui, W, Shrader, C. R., Haswell, C. A., & Hynes, R. I. 2000, ApJL, 535, L123
Fender, R., & Belloni, T. 2004, ARA&A, 42, 317
Fender, R. P., Garrington, S. T., McKay, D. J., et al. 1999, MNRAS, 304, 865
Harrison, F. A., Craig, W. W., Christensen, F. E., et al. 2013, ApJ, 770, 103
Homan, J., Klein-Wolt, M., Rossi, S., et al. 2003, ApJ, 586, 1262
Ingram, A., Done, C., & Fragile, P. C. 2009, MNRAS, 397, L101
Ingram, A., & van der Klis, M. 2015, MNRAS, 446, 3516
Jahoda, K., Markwardt, C. B., Radeva, Y., et al. 2006, ApJS, 163, 401
McClintock, J. E., Shafee, R., Narayan, R., et al. 2006, ApJ, 652, 518
Mir, M. H., Misra, R., Pahari, M., Iqbal, N., & Ahmad, N. 2016, MNRAS, 457, 2999
Mirabel, I. F., Dhawan, V., Chaty, S., et al. 1998, A&A, 330, L9
Morgan, E. H., Remillard, R. A., & Greiner, J. 1997, ApJ, 482, 993
Muno, Michael P., Remillard, R. A., Morgan, E. H., et al. 2001, ApJ, 556, 515
Muno, M. P., Morgan, E. H., & Remillard, R. A. 1999, ApJ, 527, 321
Pahari, M., Misra, R., Mukherjee, A., Yadav, J. S., & Pandey, S. K. 2013a, MNRAS, 436, 2334
Pahari, M., Neilsen, J., Yadav, J. S., Misra, R., & Uttley, P. 2013b, ApJ, 778, 136
Pahari, M., Yadav, J. S., Rodriguez, J., et al. 2013c, ApJ, 778, 46
Paul, B., Agrawal, P. C., Rao, A. R., et al. 1997, A&A, 320, L37
Paul, B., Agrawal, P. C., Rao, A. R., et al. 1998, ApJL, 492, L66
Qu, J. L., Lu, F. J., Lu, Y., et al. 2010, ApJ, 710, 836
Reid, M. J., McClintock, J. E., Steiner, J. F., et al. 2014, ApJ, 796, 2
Reig, P., Belloni, T., van der Klis, M., et al. 2000, ApJ, 541, 883
Shaposhnikov, N., Jahoda, K., Markwardt, C., Swank, J., & Strohmayer, T. 2012, ApJ, 757, 159
Shimura, T., & Takahara, F. 1995, ApJ, 445, 780
Singh, K. P., Tandon, S. N., Agrawal, P. C., et al. 2014, Proc. SPIE, 9144, 1
Stella, L., & Vietri, M. 1998, ApJL, 492, L59
Taam, R. E., Chen, X., & Swank, J. H. 1997, ApJL, 485, L83
Wilms, J., Allen, A., & McCray, R. 2000, ApJ, 542, 912
Yadav, J. S. 2001, ApJ, 548, 876
Yadav, J. S. 2006, ApJ, 646, 385
Yadav, J. S., Agrawal, P. C., Antia, H. M., et al. 2016, Proc. SPIE, 9905, 99051D
Yadav, J. S., Rao, A. R., Agrawal, P. C., et al. 1999, ApJ, 517, 935
Zhang, W., Giles, A. B., Jahoda, K., et al. 1993, Proc. SPIE, 2006, 324
Zhang, W., Jahoda, K., Swank, J. H., Morgan, E. H., & Giles, A. B. 1995, ApJ, 449, 930